

A complete fs-laser-ablation route to miniaturized single-crystal PMN-PT piezoelectric actuators

Menotti Markovic¹, Lucia Oberndorfer¹, Tobias M. Krieger², Ievgen Brytavskyi², Barbara Lehner², Julia Freund³, Vishnu Prakash Karunakaran^{1,2}, Dorian Gangloff⁴, Christian Schimpf⁴, Peter Michler⁵, Simone Luca Portalupi⁵, Michael Jetter⁵, Rinaldo Trotta⁶, Javier Martín-Sánchez⁷, Armando Rastelli², Fadi Dohnal¹, Sandra Stroj¹

¹ *Research Center for Microtechnology, Vorarlberg University of Applied Sciences, Hochschulstraße 1, A-6850 Dornbirn, Austria*

² *Institute of Semiconductor and Solid State Physics, Johannes Kepler University, Altenbergerstraße 69, A-4040 Linz, Austria*

³ *Department of Theoretical Physics, University of Innsbruck, Technikerstraße 21A A-6020 Innsbruck*

⁴ *Cavendish Laboratory, University of Cambridge, J.J. Thomson Avenue, Cambridge, CB3 0HE, UK*

⁵ *Institute of Semiconductor Optics and Functional Interfaces, University of Stuttgart, Stuttgart, Germany*

⁶ *Department of Physics, Sapienza University of Rome, Piazzale A. Moro 5, 00185 Rome, Italy*

⁷ *Department of Physics, University of Oviedo, C/ Federico García Lorca nº 18, 33007, Oviedo, Spain*

Abstract: This article presents a novel fabrication route for miniaturized piezoelectric actuators that relies exclusively on processes based on femtosecond (fs) laser ablation. Previous work has already demonstrated that fs-lasers are uniquely suited for the fabrication of piezoelectric actuators based on PMN-PT, which are required for multiaxial strain-tuning of quantum dots (QDs) to enable, e.g. the generation of highly entangled photon pairs. Building on these foundations, the present work advances actuator performance and capabilities by introducing a local thinning strategy. This approach allows the realization of smaller devices, which in turn enables lower operating voltages, while simultaneously offering the possibility of integrating multiple quantum light sources on a single chip. The article provides a detailed description of the full fabrication chain, entirely based on fs-laser processing steps, from substrate thinning to metal layer structuring and final device definition. A particular focus is placed on the final cutting process, where the implementation of a third-harmonic ultraviolet (UV) fs-laser wavelength significantly improves edge quality and shape definition compared to the second harmonic (SH) wavelength used in previous work. The device fabricated through the combination of local thinning and UV-based cutting promises not only to enhance the efficiency of strain transfer but also to ensure the mechanical stability required for practical applications.

These results establish fs-laser-based fabrication as a versatile and scalable method for next-generation piezoelectric actuators, paving the way for advanced strain-engineering approaches in semiconductor quantum optics and integrated quantum photonics.

Keywords: femtosecond laser, piezo actuator, laser micro structuring, laser ablation, PMN-PT, strain-tuning, quantum dot

1. Introduction

Piezoelectric materials play a crucial role in Micro-Electro-Mechanical Systems (MEMS) due to their unique ability to convert mechanical into electrical energy and vice versa. This property makes them particularly suitable for applications in sensors and actuators. Notable advantages of these materials include a large dynamic range, low power consumption, and minimal hysteresis values [1]. Among the various piezoelectric materials, lead magnesium niobate-lead titanate (PMN-PT) in single crystal

form stands out due to its exceptionally high piezoelectric constant (d_{33}) and coupling factors, as well as its high sensitivity. These characteristics facilitate its use in high-quality sensors and actuators [2] [3] [4].

In addition to their applications in MEMS, PMN-PT materials are also utilized in ultrasound technology, where high sensitivity and a wide bandwidth are essential for producing recognizable imaging [5] [6] [7]. Notably, PMN-PT materials maintain their effective performance even at cryogenic temperatures, making them suitable for applications in low-temperature environments [8].

The precise controllability and high piezoelectric response of PMN-PT makes it an ideal material for the realization of actuators for strain-tuning of quantum dot emitters. Strain influences the band structure and optical properties of semiconductors. The ability to introduce deliberate in-plane strain fields in semiconductor quantum dots opens exciting possibilities such as the production of polarization entangled photons via tuning of the fine structure splitting in the biexciton-exciton decay [9]. However, this application requires a complex multi-axis actuator which can be operated at cryogenic temperatures.[10], [11], [12], [13].

As actuators based on single crystal PMN-PT are particularly delicate due to their brittleness, small dimensions and thin substrates, processing options are very limited. Moreover, special processing methods are required to bring the PMN-PT substrate into the appropriate shape, as required for multi-axial strain tuning. Properties such as a resolution in the micrometer range, arbitrary geometries, low surface roughness and sharp edges must be fulfilled in order to achieve repeatability, reliability of the function, as well as yield.

Various processing techniques have been employed for structuring and cutting PMN-PT substrates. These are wet etching [14], dry etching [15] [5], reactive ion etching [16] or ion milling [3], [17]. Each process has its advantages, but also limitations such as long processing times, limited geometric possibilities or insufficient processing quality. Laser ablation in general offers a flexible direct writing process with good process times and the potential for high quality devices [15], [18], [19], [20].

In our previous work on the processing of PMN-PT and applications of the actuators in the field of semiconductor-based quantum optics, we were able to demonstrate the high potential of femtosecond laser processing [21]. Actuators of various geometries were realized by laser cutting with the second harmonic of the femtosecond laser at 523 nm. In addition, the individual electrical contacts were patterned by selective ablation of a gold layer using the same laser source. In this way, devices with a total thickness of 300 μm and a side length of 5 mm were developed. The minimum distance between the individual actuator arms was limited to 30 μm due to the laser parameters and the sample thickness.

Current research efforts in the field of quantum emitters focus on higher integration density, which leads to a need for miniaturized actuators. To ensure comparable strain-transfer properties, our new design strategy incorporates localized thinning of the active regions, as illustrated in Fig. 1. This approach offers the advantage of achieving higher electric fields at the same applied voltage while maintaining mechanical stability via the thicker surrounding areas. Additionally, laser cutting within these thinned regions enables the realisation of narrower cutting widths and potentially higher strain amplification. However, this new generation of actuators leads to a more complex manufacturing workflow compared to the previously published strain-tuning platforms. For the final device, it is critical that the fabrication produces clean, defect-free surfaces – without debris, cracks, or fracture points – as these affect its functionality during use.

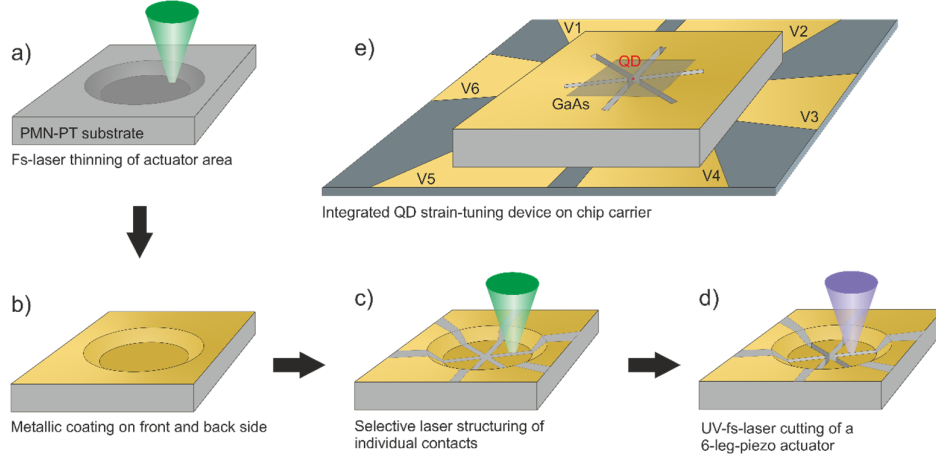


Fig. 1 The schematic diagram shows the process workflow for realising locally thinned piezo actuators using fs-laser ablation and a sketch of a strain-tuned quantum emitter. In the first step, the 300 μm thick single-crystal material is locally thinned (a) using the second harmonic of the femtosecond laser. Then, thin metal layers are vapour-deposited on the front and back side (b). These serve as an electrical ground on the bottom and contacts for the individual actuator arms on the top side. An intact conductive layer over the cavity edges is important to ensure reliable control of the individual actuator arms. After structuring of the front contacts by means of selective ablation (c), the actuator is finally created using UV-fs-laser cutting (d). (e) Sketch of a 6-legged actuator for multiaxial strain tuning of a QD embedded in a GaAs nanomembrane bonded on its top surface. Six independent voltages (V1- V6) are applied to the individual legs at the bottom of the actuator by contacting each of the legs on a chip carrier.

This work covers the development of the process steps for thinning (Fig. 1a), contact layer structuring (Fig. 1c), and UV cutting (Fig. 1d). In addition to the development of the laser processes, the influence of the metal layer thickness on the conductivity over the non-planar areas is explored (Fig. 1b). The final integration of the actuator (see Fig. 1e) is identical to previous work, with the difference that local thinning creates a space between the PMN-PT and the chip carrier in the active area. This is an improvement as the free movement of the individual arms is always guaranteed.

Compared to actuators in previous work [22], the experimental design was miniaturized in terms of lateral diameter and cutting width. It consists of two symmetrical sides with two cantilevers (arms) and a center bar, a configuration which enables the individual manipulation of strain in two regions in close vicinity to each other.

2. Experimental

The material used for all experiments was x2b from TRS ceramics with a thickness of 300 μm . A femtosecond laser source (Spirit^(R) 1040-HE from Spectra Physics) with a pulse duration of 330 fs (260 fs @ SH) was used for the ablation experiments. The laser is integrated in a micromachining system “microstructVario” from 3D Micromac. For most experiments the second harmonic at a wavelength of 523 nm was used. The beam was focused and manipulated using a galvo scanner with a lens of $f=170$ mm focal length. The cutting experiments were performed with the third harmonic (UV) wavelength at 348 nm using a $f=160$ mm lens. The beam radius was determined with the method of Liu et al. [23] and was 11 μm for the 523 nm wavelength and 6 μm for the UV wavelength, respectively. A repetition rate of 100 kHz was used for all thinning and layer structuring experiments. The UV cutting experiments were performed with a repetition rate of 250 kHz. The substrates were coated using vacuum evaporation with an e-gun. The machine used was a Balzers BAK 550 with ESQ 110 e-gun. The source material was held in a water-cooled graphite crucible. The profile measurements of cavities were done with a Keyence VK-X250 Laser scanning microscope.

3. Results

3.1 Generation of cavities with freely adjustable sidewall angles

As the first step of the actuator fabrication process, the PMN-PT substrate with a thickness of 300 μm has to be thinned down to a residual thickness of 100 microns within the area of a circle (see Fig. 1b). Thinning is realized by scanning the laser along parallel lines with a distance of 5 microns resulting in a pattern which is repeated until the final depth is reached. In order to achieve a uniform removal with a minimal surface roughness, the scanning pattern is rotated by a random value after each repetition. This ensures that line intersections are statistically distributed over the surface. For a specific set of laser and structuring parameters, the ablation depth per repetition was determined. For this, the depth of a cavity was measured after a repetition number of $N=200$ using an optical microscope which resulted in a value of 150 μm . Based on this measurement there is a focus shift of $150 \mu\text{m}/N=0.75 \mu\text{m}$ applied after each repetition for all following experiments. This focus shift leads to a constant fluence value on the substrate surface during the machining process and results in a simple linear relation between ablation depth and number of repetitions which is shown in Fig. 2a.

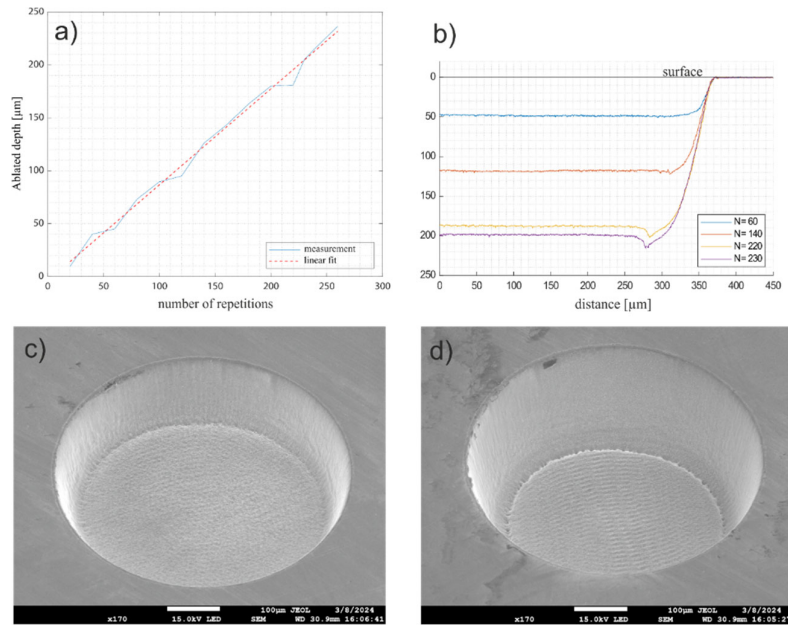


Fig. 2 Panel (a) shows the linear dependence of the depth removed per scan repetition. Measurements of the cavity profile for different repetition values using a confocal microscope show indentations at the transition from the base to the side edge (b). This becomes more and more pronounced as the number of repetitions increases. Panels (c) and (d) show SEM images of the cavity at $N=140$ and 220 , respectively. After 140 repetitions, the first signs of irregularities forming along the side edge can already be seen. After 220 , a clear ring with significant indentations has already formed.

In order to investigate the profile geometry, measurements using a Laser Scanning Microscope (LSM) have been carried out, the results can be seen in panel b of Fig. 2. The cavities were measured after machining with a selection of passes at $N = 60, 140, 220$ and 230 . In all cases one can see that the bottom plane is parallel to the substrate surface, indicating uniform removal. The transition from the ground to the side edge forms a radius due to the Gaussian beam profile, as clearly visible after a repetition number of $N=60$. An increased roughness in this area can already be recognized in the measurement at $N=140$. After $N=220$ and higher, one can clearly see pits in this transition region. Panels c and d show SEM images of the cavities created with $N = 140$ and $N = 220$, respectively. They clearly show an increased roughness in the measurement and the beginning of the formation of small holes along the sideline. By increasing the number of repetitions, these holes become even more pronounced and form a recessed ring around the bottom surface. This effect is well known and has already been reported [24], [25]. It is most likely caused by reflections at the side edge, as discussed by Toenshoff and co-authors during their research on femtosecond silicon cutting [26]. The reflections lead to an increased intensity in the edge area and the formation of the indentation. The

profile measurements also show that the sidewalls form an inclination angle of approximately 13°, despite using the same diameter for each repetition. This can be attributed to the increase of the laser beam's area projected on the sidewalls at larger depths, which in turn reduces the fluence to the level of the threshold fluence, hence no further ablation occurs [27].

To suppress the formation of the trenches along the sideline and to investigate the influence of various scanning patterns on the resulting cavity geometry, the following strategies were applied:

- large to small (LTS), where the diameter of the circular hatch pattern is decreased for each repetition
- small to large (STL), where the diameter is increased for each repetition
- random (RND), where the diameter is randomly chosen between a maximum and minimum value for each repetition

Each strategy was processed with the same parameters listed in table 1.

Wavelength	523 nm
Lens, focal length	170 mm
Repetition rate	100 kHz
Markspeed	1000 mm/s
Power	0.45 W @ 100 kHz
Focussshift	-0.75 μm for each repetition
Polarisation	Circular
Cavity diameter	500 μm

Table 1: Process parameters for the generation of the cavities

All thinning strategies (LTS, STL and RND) were followed with the same parameters from table 1 using 230 repetitions, which led to cavities with a depth of 200 μm. Just the diameter of the circle was changed for each repetition. Thus, the difference in surface quality and geometry is solely attributed to the scanning strategy applied.

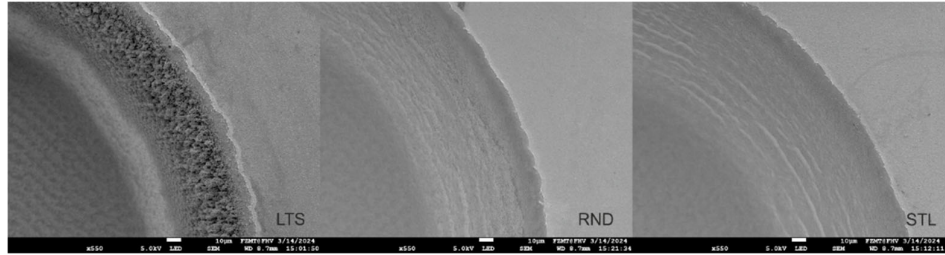


Fig. 3 SEM images of sections of cavities processed with three different scanning strategies. On the left image (LTS) the diameter of the ablation pattern decreases with every pattern repetition. In case of RND the diameter of the pattern is randomly chosen between two values and in case of STL the diameter increases during processing.

The inner and outer diameters (450 μm and 500 μm) were chosen in a way that they correspond to the inclination angle of the side wall that could already be observed in the previous tests. Fig. 3 shows SEM images of sections of the cavities. The transition from the bottom surface to the sidewall shows that the formation of the trenches was suppressed with all three methods. This confirms the assumption that the cause of their formation are reflections of the laser beam at the side edge. In all three variants, the passing over this area was reduced. In the area of the side edge, a deterioration in the edge quality can be clearly recognised in the case of LTS. The edge shows a high surface quality in the lower area of the cavity. Moving upwards, an increasing amount of deposits accumulate towards the upper edge. By reducing the scanning area after each repetition, the debris are deposited more and more in the outer areas. With the RND and STL methods, these deposits cannot be observed as any existing deposits are constantly removed from the side edge by repetitions with a larger

diameter. In general, the RND and STL methods show similar morphologies with comparable surface roughness.

With these two selected strategies, RND and STL, experiments were conducted where the inner diameter was varied for each cavity. These span from 350 μm to 450 μm with steps of 20 μm , with the aim to examine possible variations of the sidewall angle. This is particularly important for applications of PMN-PT as actuators where electrical contacts are realised through vapor deposition of a thin metal layer on the surface. Here, the sidewall angle and the surface quality have a decisive impact on the conductance of the layer in these critical areas.

The cavity profiles realized in this way were again measured using the laser scanning microscope. The results can be seen in the graphs of Fig. 4. In general, only a slight change in the sidewall angle can be observed as a function of the inner diameter. The values deviate significantly from the ones expected from geometric calculations and are comparable for both methods. A possible explanation for the low variation in flank angles is that for low changes in diameter (less than 1 micron) the angles and the profile are influenced predominantly by the gaussian profile of the beam rather than geometrical parameters.

A difference between the RDN and the STL method can be observed in the formation of the bottom surface.

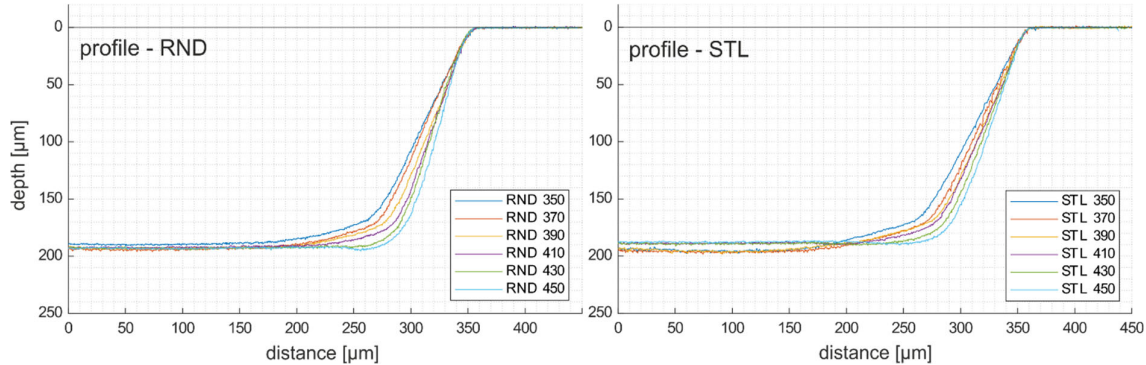


Fig. 4 Profiles of cavities with varied inner diameter. The angles show small variations

For parameters that lead to steeper edge angles, RND shows a slight indentation in the corner region, whereas with the STL method, the entire bottom surface shows a uniform depth. However, with smaller inner diameters, this method shows a significantly more curved bottom surface compared to RND.

In order to further examine the possible variation in flank angles towards significantly lower values, cavities were generated by applying the same parameters as in table 1 but with the chosen geometry altered. Instead of using a circle, a rectangle with 500 microns in width and 2.5 mm in length was chosen. The rectangle was then shifted by a fixed value from left to right for each of the 200 repetitions. The values range from 0 to 10 μm , with a step of 1 micron. In total, 11 cavities were generated with this method. By using this scheme, the left side resembled LTS, while the right side resembled STL. Fig. 5 shows the results for the left and right side of 3 cavities with a shift value of 1, 2 and 5 microns, respectively.

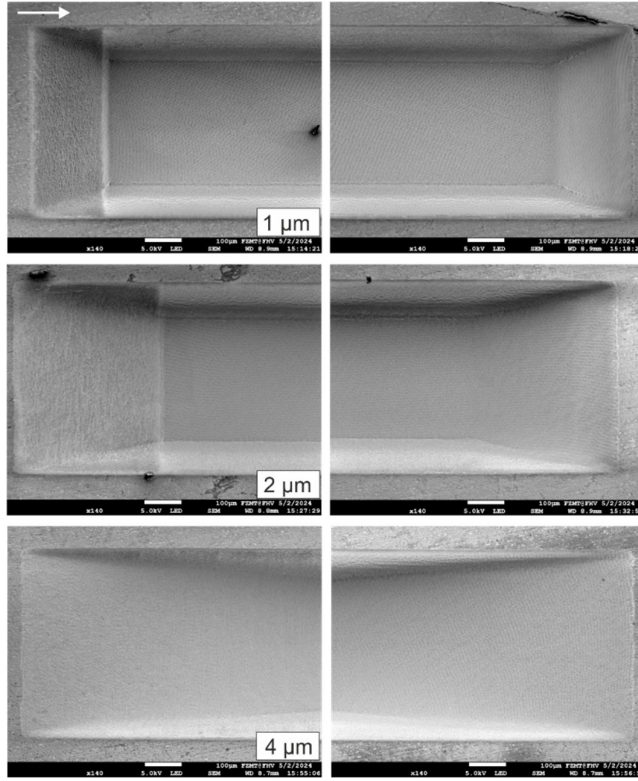


Fig. 5 SEM images of left and right ends of cavities realised with shift values of 1 μm (top), 2 μm (middle) and 4 μm (bottom line)

As moving the pattern to the right means that the machined surface on the left is no longer passed by the laser, debris is expected to be deposited on the side edge. The reduced surface quality can be recognised at a pattern shift value of 1 μm . However, the amount of accumulations is already reduced significantly compared to the previous tests, which correspond to a shift of 0.11 μm . The right ends show a good quality for all parameters, similar to STL. Additionally, it is clearly visible that the flank angles can be varied in a larger range than the previous experiments show. The corresponding profile measurements are presented in the left panel of Fig. 6.

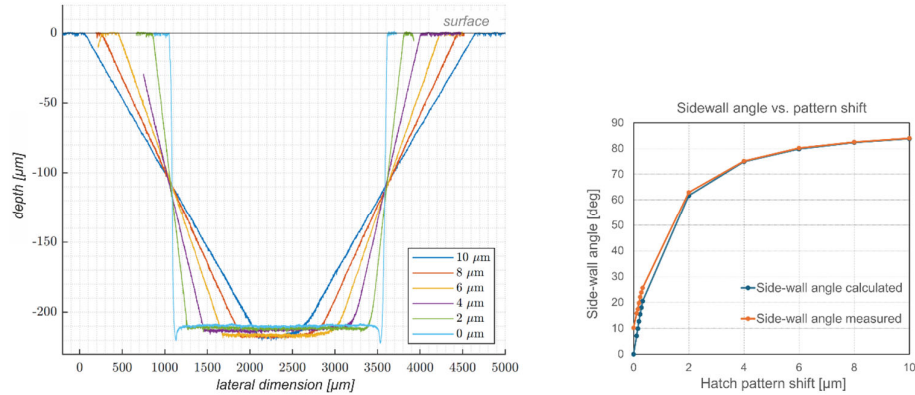


Fig. 6 left: Measurement of the cavity profile for different values of pattern shift showing straight lines with no influence of the shift direction on the sidewall angle; right: A comparison of the measured sidewall angle with the estimated value. The angles correspond for offset values higher than 4 μm .

The profile measurements demonstrate clearly that it is possible to generate cavities with a larger variety in flank angles. It can also be seen that, if the pattern is moved constantly, an inclined plane of the same angle is formed on both the left and right side. In addition, the resulting angle corresponds exactly to the calculated value for pattern shift values higher than 4 μm . Above this value, the influence of the Gaussian beam profile which leads to higher angles as expected is no longer observable. This makes it possible to realize quasi-3D structures (limited to non-undercut geometries) by laser thinning with adapted hatch layers. Since the geometry of the side wall in terms of shape and angle is independent of the processing method, there is a clear difference in case of the bottom edge. A rounded edge forms on the left which is of comparable dimensions as the laser beam. On the right, there is a smooth transition from the bottom surface to the sidewall with a significantly higher radius. We assume that the reason for the difference in radius lies in the different geometrical starting points. When the rectangle is shifted to the right with each repetition, the ablation on the left side always occurs on a flat surface, finally creating a sharp edge. Contrary to that, the ablation on the right side always occurs over the end of the previous ablated surface and thus on an uneven surface condition. This leads to ablation with reduced fluence in this area, which does not affect the final sidewall angle but does lead to a rounding of the geometry at the bottom edge.

3.2 Realisation of conducting paths beyond laser thinned areas

In order to electrically control all, even thinned areas of the piezo, we must be able to apply a continuous conductive layer over the previously processed surfaces. Since the non-even metallization layer cannot be patterned easily by standard lithography methods, it is subsequently structured by means of selective laser ablation to form individual areas for actuator control. To prepare the substrate for evaporation tests, it was first thinned using the parameters for the circular hatch pattern with a variation of the inner diameter. After a cleaning step with deionized water and subsequent treatment in oxygen plasma the samples were coated with titanium in steps. During each coating process, 25 nm with a deposition rate of 1.5 Å s^{-1} were deposited onto the surface while the substrate was rotated within the machine. For final applications, a gold coating is preferred due to its significantly higher conductivity. However, these tests were carried out with Ti due to its higher adhesion. This reduces the risk of delamination of the individual layers as the process was interrupted several times for the conductivity measurement. The resistance was measured using tungsten needles, which are connected to a multimeter; one was placed on the bottom of the cavity, while the other one was placed at the top surface. The resistance was measured between these two points, the results for both thinning strategies can be seen in Fig. 7.

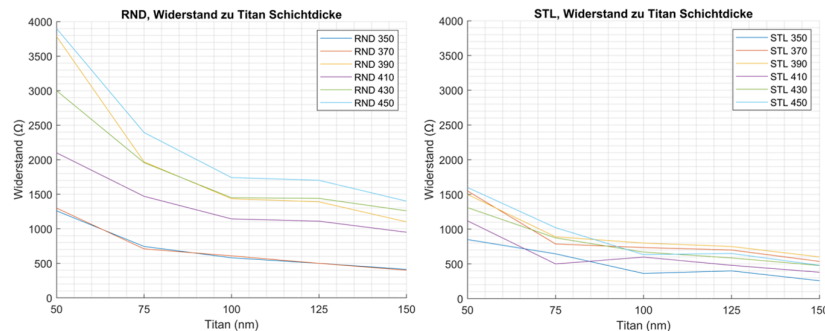


Fig. 7 Electrical resistance measurements for various layer thicknesses of Ti for cavities generated with varying inner diameters (indicated in the legend) using the RND (image on the left) and STL (image on the right) method.

Although the methods RND and STL showed comparable results regarding morphology (Fig. 4), the slight differences in edge geometry leads to significant variations in the conductance of the deposited metallic layer. Particularly in the case of steeper edges, the cavities realized with the RND method exhibit considerably higher values of electrical resistance. While these values decrease as the layer thickness increases, they remain higher compared to STL. The difference is likely due to the

noticeable indentation at the side edges in the case of RND, which seems to have a direct impact on the layer conductivity in this region. As a result of these measurements further examinations regarding layer structuring were continued with cavities fabricated using the STL method.

Circular cavities were generated for the tests to create structured metallic contacts on non-planar surfaces. Inner diameters of 350 μm and 450 μm were chosen, resulting in the smallest and largest values for the sidewall inclination, as demonstrated in **Error! Reference source not found.** After a cleaning step, a coating of 10 nm titanium and 150 nm gold was applied. After that, a rectangular structuring path was ablated using the femtosecond laser, with one of the long sides placed centrally over the cavity (see schematic of Fig. 8). After structuring, the electrical separation between the inner and outer surfaces of the rectangle was tested both on the cavity floor and on the substrate surface. In addition, the conductivity from the bottom to the top surface was also measured as in the coating tests.

One characteristic of ablation with ultrashort laser pulses is a sharply defined ablation threshold. This was measured using Liu's method [23] and is 0.14 J/cm² in the case of gold and 0.45 J/cm² for PMN-PT for a pulse duration of 350 fs at a wavelength of 523 nm. These values show the potential for selective structuring of gold on PMN-PT, which we demonstrate below.

For the layer structuring, a repetition rate of 100 kHz and a processing speed of 700 mm/s were selected. Different samples were structured with power values of 0.882 W and 0.788 W, all with 2 and 3 pattern repetitions. The focus was positioned to half the depth of the cavity. This provides the highest possible value for the intensity at the side edge. This is advantageous as the fluence value is smaller compared to flat surfaces due to projection onto an inclined plane. The Rayleigh length of the focused beam is 696 μm and is considerably higher than the depth of the structure.

Electrical resistance between separated areas on the floor, as well as on the substrate surface, should be very high. Measurements show that each combination of power values and repetitions (8 in total) results in a resistance value exceeding the maximum possible measurement value of 50 M Ω for the multimeter used. In addition, the resistance of the gold layer over the side edge, as carried out in the coating tests, was also examined which resulted in values between 3 and 9 Ω for all samples. The SEM image in Fig. 8 shows the result of the structuring process at a laser power of 0.882 W and a repetition number of three. The slight difference in the shade of grey inside and outside the rectangle, which is due to different electrical charges, already visualises the distinct electrical properties of these areas. The measuring points for conductivity are also shown schematically.

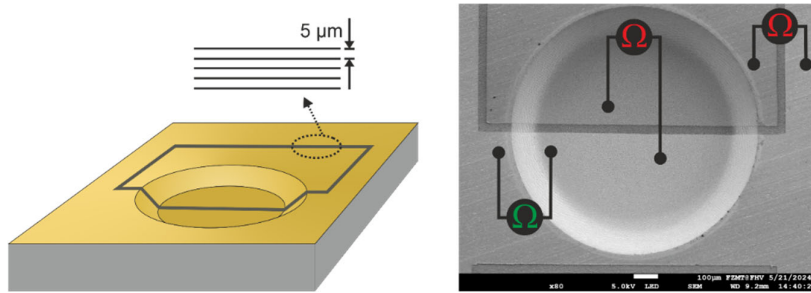


Fig. 8 Schematic of the laser-structured Au-layer (left side) showing the rectangular separation path placed beyond the cavity. To obtain a certain path width, 5 parallel lines with 5 μm distance were applied. The laser power was 0.88 W and the pattern was repeated three times. The SEM image on the right side shows a clear removal of the thin gold layer. The slight difference in the shade of grey inside and outside the rectangle, which is due to different electrical charges, already visualises the electrical separation of these areas. The measurement points for conductivity determination are also marked in the SEM image.

3.4 UV laser cutting within the locally thinned areas

PMN-PT based piezo platforms realized by laser cutting for quantum optical applications has already been successfully demonstrated [28], [29], [30]. The cutting process was based on the creation of equidistant lines to the cutting path geometry with variable line spacings. Process parameters like fluence and repetition rate were within a narrow process window allowing cutting with minimal thermal stress on this very sensitive material. Regarding the influence of the wavelength, the laser was

operated at a wavelength of 523 nm. However, if the actuator design is subjected to a further reduction in size as it is in this work, these process parameters are no longer applicable and need to be adjusted to achieve the precision requirements. For this reason, a new approach is chosen in this study.

As a first change in the parameter set, the wavelength of the laser was reduced to the third harmonic at 348 nm. This provides the advantage of a smaller spot radius on the one hand and improved absorption conditions on the other. Data from the literature determine the band gap of monocrystalline PMN-PT with a value in the range of 3.1 to 3.3 eV, depending on material composition and temperature [31]. This is just between the photon energy of the laser at its second (2.37 eV) and third harmonic (3.56 eV), respectively. For this reason, the energy can be deposited by linear absorption using the UV wavelength in contrast to the previously used cutting process, where one had to rely on a two-photon absorption mechanism. This has the advantages of an intensity-independent deposition of energy within the optical penetration depth and, as a consequence, of a reduced effect to the adjacent bulk material.

As already mentioned, the refined actuator concepts are based on a locally thinned area in which a miniaturised design is realised using the UV fs-laser. However, as PMN-PT is difficult to manipulate mechanically at this greatly reduced thickness of 100 μm , a substrate with a thickness of 300 μm was used for the first tests to evaluate the cutting edge. To refine the process parameters and evaluate the laser exit edge, the substrates were thinned to the reduced thickness of 100 μm using laser thinning as described in section 3.1.

The SEM images in Fig. 9 show the design of a three-unit actuator, realised with different power values and variable number of passes. Two sets of equidistant lines were applied alternately to achieve the required cutting depth. First, 10 lines were applied with a distance of 4.5 μm to ensure removal even at the wider parts of the geometry, so that there were no free-standing parts at the end of the cutting process. Then, additional equidistant lines with reduced distance (5 \times 2 μm) should lead to a more distinctive cutting edge.

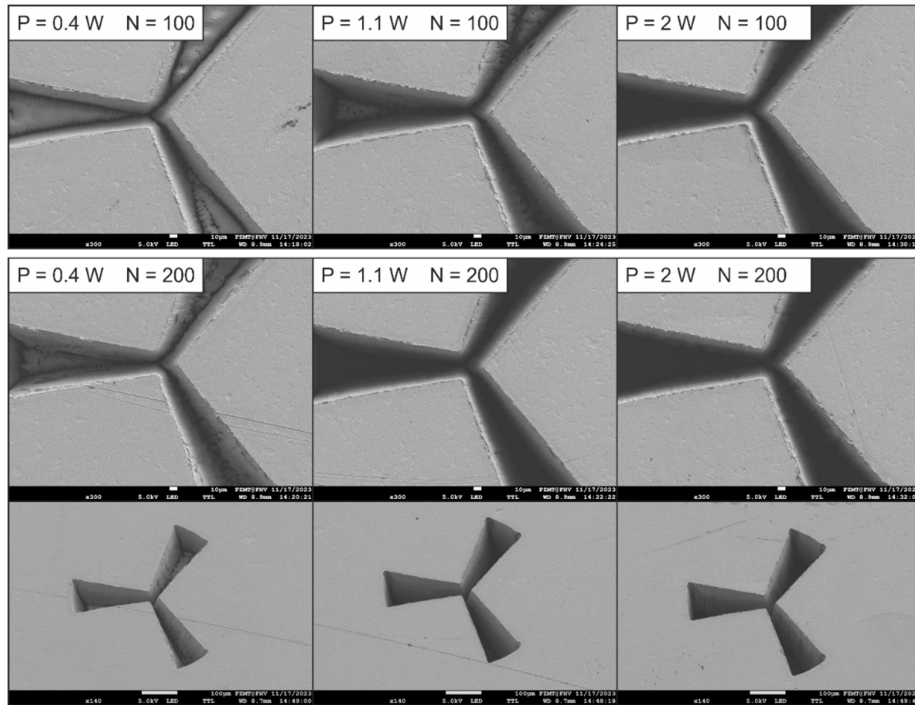


Fig. 9 SEM images of a three-leg actuator design cut with different laser and process parameters using the third harmonic wavelength. For the process, two sets of equidistant lines were applied; 5 lines with a distance of 2 μm and 10 lines with a distance of 4.5 μm . In the upper row results for three different values of laser power and a repetition number of 100 is shown. Row 2 and 3 show results after 200 repetition and an additional cutting design overview.

The laser was operated at a repetition rate of 250 kHz. The scanner speed was 1250 mm/s for all tests. The results shown in the upper row were obtained with a repetition of the cutting line pattern of 100. It can be clearly seen that the ablation depth is very low, especially at a power of 0.4 W. The arrangement of the cutting lines creates a cushion-shaped base inside the cutting geometry. This leads to a very clear depression along the actual cutting line. If the laser power is increased, the ablated depth is considerably higher, although the quality of the edges hardly shows any change. At a repetition of 200, the base area can only be seen at the lowest power of 0.4 W. The further course of the edge can no longer be evaluated. Evaluating the cutting edge on the laser entrance side shows a high quality with no evidence of any breakouts for the power value of 1.1 W. Since there is slight melting recognized at 2 W, the following tests will be performed with the power value of 1.1 W.

To estimate the quality to be expected on the exit side, the bottom of the cavity for a power of 1.1 W at 100 repetitions can be evaluated. This already shows increasing irregularities with depth, which suggest that an adaptation of the machining strategy is required to improve the quality.

In this alternative approach, instead of performing cuts using equidistant lines, the actuator geometry is processed using a line hatch pattern with the process parameters as described in section 3.1. This allows a pre-thinning of the geometry with the highest surface quality and a flat inner area. SEM images in Fig. 10 show the actuator geometry during thinning for different values of pattern repetition. Due to the small dimensions and the Gaussian beam profile, a rounded mold is formed. Starting from a repetition of 15, slight waviness appears at the bottom of the structure. Above a repetition of 70, an irregular side edge forms at the bottom of the structure.

As a lower fluence is used when thinning compared to cutting, a cavity with a lower side edge angle is created. As already discussed in [21], the angle of the side edge depends solely on the ratio of the laser fluence to the ablation threshold of the material. It is expected that the higher fluence during cutting will widen the cavity, which should have a positive effect on the cut edge definition.

After a defined number of repetitions, the cutting procedure switches to the actual cutting process with a set of equidistant lines and higher fluence values. This is intended to improve the quality of the final cutting edge on the laser entrance as well as on the laser exit side.

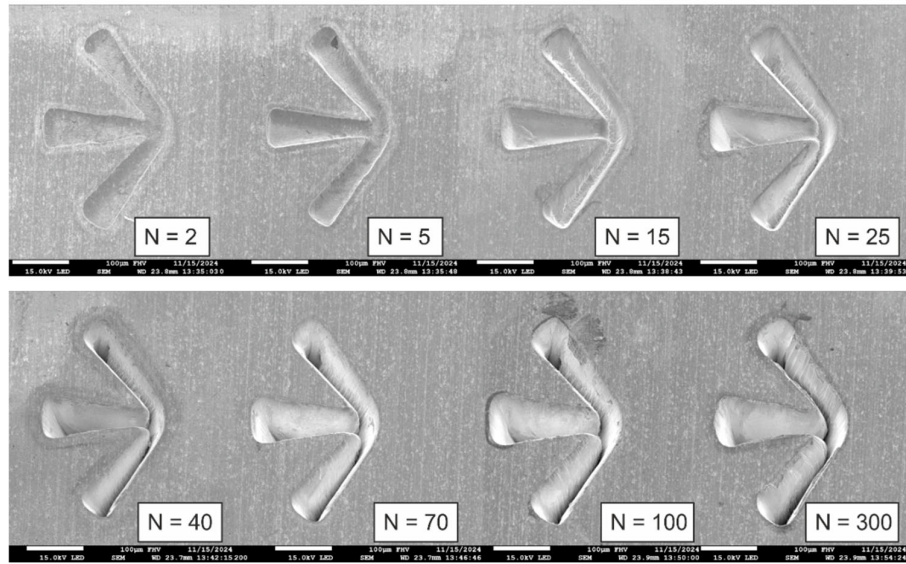


Fig. 10 SEM images of cavities generated by a line hatch pattern for an increasing number of pattern repetitions. As the number of repetitions increases, a rounded mould first forms, which deepens more and more and develops into a cut edge for repetitions higher than 40. A trough formation in the ablation is already recognisable from the 5th repetition, which transforms into a trench from the 15th repetition. The lateral flanks become increasingly steep and misshapen.

In preparation for the final cutting tests, circular cavities with a residual thickness of 100 μ m were created. A geometrically split actuator, each side with two electrically controllable arms, is realised in

these cavities. In preparation for the process, the substrate is bonded to a ceramic sample holder using polyvinyl alcohol (PVA). Care is taken to ensure that both the front and the back side of the piezo substrate are fully covered with the coating. This is necessary in order to be able to remove deposits from the cutting process together with the PVA layers.

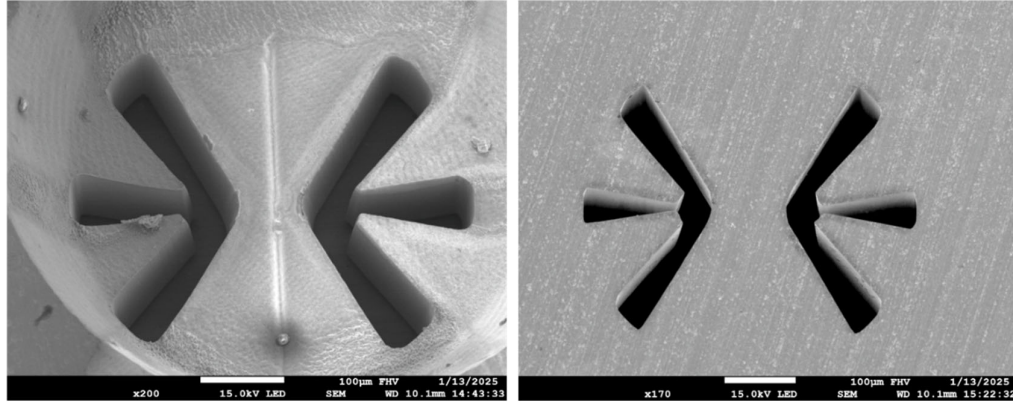


Fig. 11 SEM images of a UV-laser cut actuator, processed within a laser-thinned area with residual sample thickness of 100 μm . The smallest inter-arm distance on the laser exit side is with a value of just 5 μm a significant reduction compared to actual designs realised with the SH wavelength. This has a direct effect on the achievable strain values with this new approach. Additionally, the lack of any irregularities on the back side of the actuator is crucial for subsequent bonding of the quantum emitter devices on this strain tuning platform.

Fig. 11 shows the front and back side of the final cut actuator after the protective coating has been removed. Deposit residues can still be seen inside the cavity which can be explained by insufficient coverage with PVA.

Looking at the cut, a sharp, well-defined edge can be seen on both the laser entrance and the exit side. The exit side in particular is very critical for subsequent processes, as this is where the semiconductor membrane containing the quantum emitters is to be bonded. The SEM image on the right does not show any elevations or breakouts at the edges of the cut regions. This is a decisive improvement compared to the results with the second harmonic wavelength. If one compares the cut width at the exit side with 5 μm at the smallest point in comparison to 10-15 μm achieved with SH, a significant reduction is also possible through the use of UV. We expect this reduced width to enable higher strain values with reduced operating voltage compared to previously used tuning platforms.

5. Conclusion

In this work, we successfully demonstrated the fabrication of miniaturized and structurally complex piezo actuators based on single crystal PMN-PT using exclusively ultrashort pulsed laser processing for local sample thinning, electrode structuring and actuator cutting. In particular, the use of UV wavelengths enabled highly precise laser cutting, which proved essential for achieving the required resolution and structural precision. The newly developed process sequence enables actuator designs that offer promising new approaches for applications in the field of multiaxial strain-tuning, such as the integration of multiple individually addressed quantum emitters or the realisation of higher and more directional strain values with miniaturized devices.

Acknowledgements

Parts of the work was funded within the QuantERA Programme that has received funding from the EU H2020 research and innovation programme under GA No 101017733 via the project QD-E-QKD and from the MUR (Ministero dell'Università e della Ricerca) through the PNRR MUR Project PE0000023-NQSTI and via the Project MEEDGARD: grant.13948955, EPSRC EP/Z000556/1 and 425333704 FWF-DFG.

J.M.-S. acknowledges financial support from the Spanish Ministry of Science and Innovation (grant number PID2023-148457NB-I00 funded by MCIN/AEI/10.13039/501100011033 and FSE+, PCI2022-132953 funded by MCIN/AEI/10.13039/501100011033 and the EU “NextGenerationEU”/PRTR, CNS2024-154342 funded by MICIU/AEI /10.13039/501100011033”)

References

- [1] J. Holterman und P. Groen, *An introduction to piezoelectric materials and applications*. Apeldoorn: Stichting Applied Piezo, 2013.
- [2] S.-E. Park und T. R. Shroud, „Ultrahigh strain and piezoelectric behavior in relaxor based ferroelectric single crystals“, *J. Appl. Phys.*, Bd. 82, Nr. 4, S. 1804–1811, Aug. 1997, doi: 10.1063/1.365983.
- [3] S.-H. Baek, M. S. Rzchowski, und V. A. Aksyuk, „Giant piezoelectricity in PMN-PT thin films: Beyond PZT“, *MRS Bull.*, Bd. 37, Nr. 11, S. 1022–1029, Nov. 2012, doi: 10.1557/mrs.2012.266.
- [4] E. Sun und W. Cao, „Relaxor-based ferroelectric single crystals: Growth, domain engineering, characterization and applications“, *Prog. Mater. Sci.*, Bd. 65, S. 124–210, Aug. 2014, doi: 10.1016/j.pmatsci.2014.03.006.
- [5] C. Liu, F. Djuth, X. Li, R. Chen, Q. Zhou, und K. Kirk Shung, „Micromachined high frequency PMN-PT/epoxy 1–3 composite ultrasonic annular array“, *Ultrasonics*, Bd. 52, Nr. 4, S. 497–502, Apr. 2012, doi: 10.1016/j.ultras.2011.11.001.
- [6] Y. Li *u. a.*, „PMN-PT/Epoxy 1-3 composite based ultrasonic transducer for dual-modality photoacoustic and ultrasound endoscopy“, *Photoacoustics*, Bd. 15, S. 100138, Sep. 2019, doi: 10.1016/j.pacs.2019.100138.
- [7] Fraunhofer Institute for Ceramic Technologies and Systems IKTS *u. a.*, „Investigations of high-Performance Ultrasonic Transducers based on PMN-PT Single Crystals“, *E-J. Nondestruct. Test.*, Bd. 29, Nr. 6, Juni 2024, doi: 10.58286/29957.
- [8] T.-B. Xu, „Review on PMN-PT Relaxor Piezoelectric Single Crystal materials for cryogenic actuators“, in *AIAA SCITECH 2022 Forum*, San Diego, CA & Virtual: American Institute of Aeronautics and Astronautics, Jan. 2022. doi: 10.2514/6.2022-2240.
- [9] J. Martín-Sánchez *u. a.*, „Reversible Control of In-Plane Elastic Stress Tensor in Nanomembranes“, *Adv. Opt. Mater.*, Bd. 4, Nr. 5, S. 682–687, Mai 2016, doi: 10.1002/adom.201500779.
- [10] R. Trotta *u. a.*, „Wavelength-tunable sources of entangled photons interfaced with atomic vapours“, *Bd. o.Jg.*, Nr. Nr. 10375, S. 7, 2016, doi: 10.1038/ncomms10375.
- [11] J. Yang, M. Zopf, und F. Ding, „Strain tunable quantum dot based non-classical photon sources“, *J. Semicond.*, Bd. 41, Nr. 1, S. 011901, Jan. 2020, doi: 10.1088/1674-4926/41/1/011901.
- [12] D. Huber *u. a.*, „Strain-Tunable GaAs Quantum Dot: A Nearly Dephasing-Free Source of Entangled Photon Pairs on Demand“, *Phys. Rev. Lett.*, Bd. 121, Nr. 3, Juli 2018, doi: 10.1103/physrevlett.121.033902.
- [13] J. Martín-Sánchez *u. a.*, „Strain-tuning of the optical properties of semiconductor nanomaterials by integration onto piezoelectric actuators“, *Semicond. Sci. Technol.*, Bd. 33, Nr. 1, S. 013001, Jan. 2018, doi: 10.1088/1361-6641/aa9b53.
- [14] J. Peng, C. Chao, J. Dai, H. L. W. Chan, und H. Luo, „Micro-patterning of 0.70Pb(Mg1/3Nb2/3)O3–0.30PbTiO3 single crystals by ultrasonic wet chemical etching“, *Mater. Lett.*, Bd. 62, Nr. 17–18, S. 3127–3130, Juni 2008, doi: 10.1016/j.matlet.2008.02.003.
- [15] I. A. Ivan, J. Agnus, und P. Lambert, „PMN–PT (lead magnesium niobate–lead titanate) piezoelectric material micromachining by excimer laser ablation and dry etching (DRIE)“, *Sens. Actuators Phys.*, Bd. 177, S. 37–47, Apr. 2012, doi: 10.1016/j.sna.2011.09.015.
- [16] J. Zhang, W. Ren, X. Jing, P. Shi, und X. Wu, „Deep reactive ion etching of PZT ceramics and PMN-PT single crystals for high frequency ultrasound transducers“, *Ceram. Int.*, Bd. 41, S. S656–S661, Juli 2015, doi: 10.1016/j.ceramint.2015.03.258.
- [17] Y. Chen *u. a.*, „Addressable and Color-Tunable Piezophotonic Light-Emitting Stripes“, *Adv. Mater.*, Bd. 29, Nr. 19, S. 1605165, Mai 2017, doi: 10.1002/adma.201605165.

[18] Z. Lei *u. a.*, „Micromachining of High Quality PMN–31%PT Single Crystals for High-Frequency (>20 MHz) Ultrasonic Array Transducer Applications“, *Micromachines*, Bd. 11, Nr. 5, S. 512, Mai 2020, doi: 10.3390/mi11050512.

[19] J. Lv *u. a.*, „Cold ablated high frequency PMN-PT/Epoxy 1-3 composite transducer“, *Appl. Acoust.*, Bd. 188, S. 108540, Jan. 2022, doi: 10.1016/j.apacoust.2021.108540.

[20] K. H. Lam, Y. Chen, K. Au, J. Chen, J. Y. Dai, und H. S. Luo, „Kerf profile and piezoresponse study of the laser micro-machined PMN-PT single crystal using 355nm Nd:YAG“, *Mater. Res. Bull.*, Bd. 48, Nr. 9, S. 3420–3423, Sep. 2013, doi: 10.1016/j.materresbull.2013.05.025.

[21] G. Piredda *u. a.*, „Micro-machining of PMN-PT crystals with ultrashort laser pulses“, Bd. 125. Jg., Nr. H. 3, S. 11, 2019, doi: 10.1007/s00339-019-2460-9.

[22] A. Laneve *u. a.*, „Wavevector-resolved polarization entanglement from radiative cascades“, *Nat. Commun.*, Bd. 16, Nr. 1, S. 6209, Juli 2025, doi: 10.1038/s41467-025-61460-3.

[23] J. M. Liu, „Simple technique for measurements of pulsed Gaussian-beam spot sizes“, *Opt. Lett.*, Bd. 7, Nr. 5, Art. Nr. 5, Mai 1982, doi: 10.1364/OL.7.000196.

[24] K. Bischoff, D. Mücke, G.-L. Roth, C. Esen, und R. Hellmann, „UV-Femtosecond-Laser Structuring of Cyclic Olefin Copolymer“, *Polymers*, Bd. 14, Nr. 14, S. 2962, Juli 2022, doi: 10.3390/polym14142962.

[25] Y. Zhao, Y.-L. Zhao, und L.-K. Wang, „Application of femtosecond laser micromachining in silicon carbide deep etching for fabricating sensitive diaphragm of high temperature pressure sensor“, *Sens. Actuators Phys.*, Bd. 309, S. 112017, Juli 2020, doi: 10.1016/j.sna.2020.112017.

[26] H. K. Toenshoff, A. Ostendorf, und T. Wagner, „Structuring silicon with femtosecond lasers“, gehalten auf der Photonics West 2001 - LASE, M. C. Gower, H. Helvajian, K. Sugioka, und J. J. Dubowski, Hrsg., San Jose, CA, Juni 2001, S. 88–97. doi: 10.1117/12.432500.

[27] C. Fornaroli, J. Holtkamp, und A. Gillner, „Dicing of Thin Si Wafers with a Picosecond Laser Ablation Process“, *Phys. Procedia*, Bd. 41, S. 603–609, 2013, doi: 10.1016/j.phpro.2013.03.122.

[28] M. B. Rota *u. a.*, „A source of entangled photons based on a cavity-enhanced and strain-tuned GaAs quantum dot“, *eLight*, Bd. 4, Nr. 1, S. 13, Dez. 2024, doi: 10.1186/s43593-024-00072-8.

[29] F. B. Basset *u. a.*, „Signatures of the Optical Stark Effect on Entangled Photon Pairs from Resonantly-Pumped Quantum Dots“, 2. August 2023, *arXiv*: arXiv:2212.07087. Zugriffen: 9. November 2023. [Online]. Verfügbar unter: <http://arxiv.org/abs/2212.07087>

[30] B. U. Lehner *u. a.*, „Beyond the Four-Level Model: Dark and Hot States in Quantum Dots Degrade Photonic Entanglement“, *Nano Lett.*, Bd. 23, Nr. 4, S. 1409–1415, Feb. 2023, doi: 10.1021/acs.nanolett.2c04734.

[31] X. L. Zhang *u. a.*, „Optical bandgap and phase transition in relaxor ferroelectric Pb(Mg $1/3$ Nb $2/3$)O 3 -xPbTiO 3 single crystals: An inherent relationship“, *Appl. Phys. Lett.*, Bd. 103, Nr. 5, Juli 2013, doi: 10.1063/1.4816965.